C. Zhao, S. Zhu, P. Di Lizia
Collision-Probability-based Hopping Trajectory Optimization on Hazardous Terrain of Small Bodies
Advances in Space Research, Published online 26/01/2023
doi:10.1016/j.asr.2023.01.043

Collision-probability-based hopping trajectory optimization on hazardous terrain of small bodies

Chuncheng Zhao [a, b], Shengying Zhu [a,*], Pierluigi Di Lizia [b]

[a] *School of Aerospace Engineering, Beijing Institute of Technology, 100081 Beijing, China*

[b] *Department of Aerospace Science and Technology, Politecnico di Milano, 20156 Milan, Italy*

Abstract

This paper studies the safe motion of a hopping rover on hazardous terrains of small bodies in the presence of initial state errors and dynamic parameter uncertainties. The collision probability is adopted to optimize the hopping trajectory. Firstly, the hazardous terrain is characterized by the least square median method, and the feasible path point zone is defined for hopping motion. Meanwhile, the hopping trajectory optimization is converted into sequence path point planning and optimal trajectory design problems based on the classical path planning algorithm. Then, considering the effects of errors and uncertainties, a performance index is derived to design a continuous hopping trajectory of sequence path points. Taking the collision probability as an index to indicate safety, local path points are optimized through path point decomposition and replacement strategy. Therefore, a collision-probability-based continuous optimal hopping trajectory can be generated to realize safe and precise motion. Finally, with the simulated hazardous terrain based on the small body 433 Eros, the effectiveness of the proposed method is verified by numerical analysis.

Keywords: Surface exploration, Hazardous terrain, Path point planning, Hopping trajectory optimization, Collision probability

1 Introduction

Small bodies in the solar system have become the primary research objects in the field of deep space exploration due to their importance in scientific research and the earth defense (Ge et al., 2019). Several exploration missions have been successfully carried out, such as Hayabusa (Yano et al., 2006),

* Corresponding author

E-mail addresses: chuncheng.zhao@polimi.it (C. Zhao), zhushy@bit.edu.cn (S. Zhu), pierluigi.dilizia@polimi.it (P. D. Lizia)

Hayabusa2 (Tsuda et al., 2020), Rosetta (Witte et al., 2016), and OSIRIS-Rex (Berry, et al., 2013). The OSIRIS-Rex mission used Touch-and-Go (TAG) technology to get surface samples of the small body Bennu. However, autonomous surface exploration can conduct broader exploration and acquire more valuable samples (Lange et al., 2018). The Hayabusa mission planned to use a hopping cube for surface exploration, which established a preliminary dynamic model and conducted theoretical and experimental verification of hopping dynamics (Yoshimitsu et al., 2003). Unfortunately, the deployed lander failed to land on the small body, so the hopping exploration mission has not been implemented. Hopping motion was also adopted in the subsequent Hayabusa2 mission, which successfully roamed the small body Ryugu, since it is better suited to exploring small bodies with low gravity and complex surface terrain (Yoshimitsu et al., 2003; Ulamec et al., 2011).

At present, a lot of research has been done on hopping explorations. Zhang et al. (2019, 2021) and Yu et al. (2015) investigated hopping motion dynamics by studying the surface particle motion of small bodies. The precise delivery of a rover from a main spacecraft to a selected landing area is an important step for an actual mission (Tsuda et al., 2020). Van Wal et al. (2017, 2018) analyzed the deployment of a hopping rover to the surface of small bodies, while Wen et al. (2020) studied the reachable domain after the hopping rover was deployed. Li et al. (2022) proposed the concept of a hopping return trajectory to achieve precise deployment of a lander. For the control of hopping motion with the impact between the rover and the surface, Cui et al. (2017) proposed an active hopping trajectory control algorithm based on an intelligent landing strategy. Bellerose et al. (2008) analyzed the dynamics of surface particles and studied the control of single and multi-cooperative surface rovers using the sliding mode control method. Li et al. (2020) proposed a strategy to reduce landing errors using only attitude control, and the velocity control after impact could be achieved to a certain extent by controlling the attitude of the hopping rover before impact. When the rover stops on the surface and then we want to drive it to conduct different tasks, the driving and hopping mechanisms are investigated. Kubota and Yoshimitsu (2013) summarized the different mechanisms of surface motion on low-gravity small bodies, mainly including external and internal mechanisms. In the Refs. Allen et al. (2013) and Hockman et al. (2017), a hopping rover driven by internal flywheels was studied, the mechanism for realizing hopping motion was given, and dynamic models and control methods under different motion modes were analyzed.

For a surface exploration mission with a hopping rover, motion planning and trajectory optimization

are also major research aspects because of the special surface environment. In the Ref. Kim et al. (2016) and Ushijima et al. (2017), the optimal path planning was studied when there were obstacles near the rover, and the feasible optimal path was generated by the A* algorithm. Jiang et al. (2020) used the deep reinforcement learning method to study the path planning of a hopping rover on complex terrain and presented a deep reinforcement learning structure with good convergence and stability. Shen et al. (2017) used the particle swarm optimization algorithm to study the trajectory optimization of multiple hopping rovers. Liu et al. (2017) used the convex optimization method to optimize a hopping trajectory, obtained the energy optimal trajectory, and analyzed the influence of transfer distance on trajectory optimization precision. In the Ref. Liu et al. (2021), the convex optimization method was used to design the collision-free long-distance transfer trajectory between any two points and was combined with the ant colony optimization algorithm to solve the optimal hopping trajectory sequence of multiple points. In the Ref. Kalita and Thangavelautham (2019), by solving the Lambert orbital boundary value problem in an irregular gravity field, the hopping trajectory from the initial position to the target position was obtained, and then the genetic algorithm was used to generate the optimal continuous hopping trajectory between two long-distance points.

The small body generally has complex surface topography (Saito et al., 2006), but it is difficult to get very detailed surface terrain distributions before the implementation of an actual task. The current research is mainly carried out based on the numerical simulation model of complex terrains. Tardivel et al. (2014) constructed a force model for a spherical rover on an irregular small body and used a probabilistic model to describe the surface obstacles. Hockman and Pavone (2018) studied the concept of traversability of a hopping rover, discussed hopping dynamics and the difference in traversability concepts between a hopping rover and a traditional wheeled rover, and proposed an algorithm to divide the surface into local traversable areas.

Besides the complex terrain, the velocity constraints are also needed for these missions because of the low escape velocity on the surface of small bodies. In the Ref. Upadhyay and Aguiar (2019), single and multiple hopping trajectories were designed based on minimum velocity constraints and maximum height constraints, and different hopping strategies were compared. Uncertainty is ubiquitous in various space missions, and it is necessary to consider the influence of uncertainties and evaluate the safety and precision of hopping motion. In the Refs. Shen et al. (2010) and Hu et al. (2016), the influence of model

parameter uncertainties and state errors during small body landing was considered, and an optimized landing trajectory that can effectively resist uncertainties and errors was obtained. In Ref. Hockman and Pavone (2017), the hopping path planning process with uncertainties was regarded as a Markov decision process, and the reinforcement learning algorithm was used to generate feasible continuous hopping trajectories.

In this paper, the path is a continuous line going from a starting point to an end point, the path points are successive points that are selected on the optimal path for hopping motion, and the hopping trajectory is the ballistic motion between two successive path points. Aiming at the safe motion of a hopping rover in hazardous terrain, a hopping trajectory optimization method is studied based on collision probability. Firstly, the safe motion problem on surface hazardous terrain is described, and the safety is defined when uncertainties are considered. Secondly, the hazardous terrain is characterized by the least square median method, so that the local approximate plane with terrain feature information and the feasible path point zone of hopping are obtained. Hopping path planning is carried out on the local approximate plane using traditional path planning algorithms, and sequence path points are planned by a given strategy according to hopping peculiarities. Then, considering model parameter uncertainties and initial state errors, an optimal hopping trajectory is designed. Finally, by calculating the on-orbit collision probability between the rover and the hazard terrain zone, a continuous optimal hopping trajectory is designed with sequence path points that are optimized by the set threshold. Fig.1 shows the flow of the proposed method.

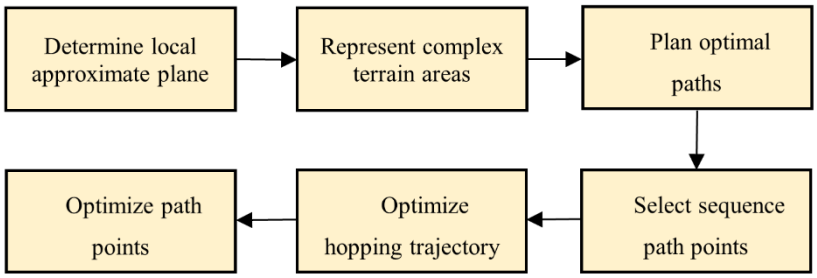

Fig. 1. Implementation steps of the proposed method

The rest of this paper is arranged as follows: Section 2 gives the dynamic model and analyzes the safety of hopping motion on hazardous terrain when uncertainties are considered. Section 3 describes how to determine the feasible path point zone, plan sequence path points, and design an optimal hopping trajectory. Section 4 gives the definition of collision probability and applies it to the optimization of hopping trajectories. In Section 5, numerical simulations are conducted to demonstrate the proposed

method based on the small body 433 Eros. Section 6 summarizes this paper.

2 Dynamics and problem statement

2.1 Surface exploration on hazardous terrain

For the surface exploration mission, it is assumed that the orbiting spacecraft first releases a landing probe onto the small body. After the probe lands, the rover is released to conduct extensive exploration and sampling on the surface. Even if the target landing area is relatively flat, there may be rock blocks, gravel piles, and pits of different sizes in the surrounding area (Saito et al., 2006; Tsuda et al., 2020). In this case of complex terrain, the motion needs to be planned based on topographic distribution to ensure safety and efficiency before the rover starts to move. This topographic information could be collected by observing the small body surface with the in-orbit spacecraft (Tsuda et al., 2020), and the reliability of motion planning will depend on the accuracy of the obtained information. If the rover adopts the hopping method, it can jump over small terrain obstacles, which can shorten the length of the motion route to a certain extent compared with the wheeled rover. The hopping motion route is determined by a series of path points, so that the motion planning on complex terrain is transformed into the planning of feasible sequence path points. After the topographic information of the target area is obtained, the obstacle zone and the feasible path point zone can be distinguished, respectively. If a start point and an end point are given, intermediate path points could be planned with terrain and motion constraints.

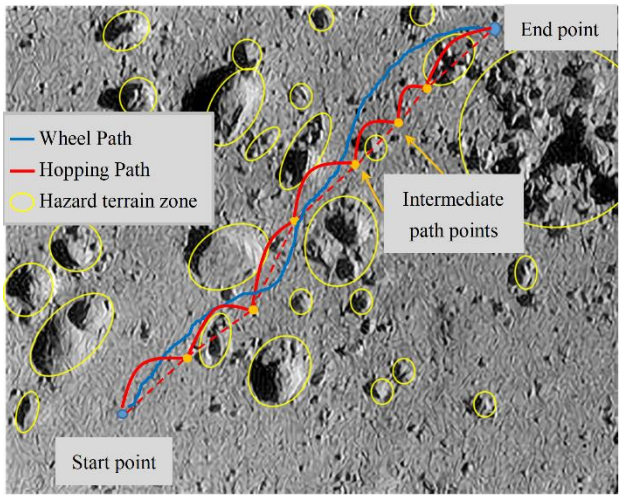

Fig. 2. Schematic diagram of two safe motion paths on hazardous terrain

The schematic diagram of the continuous hopping trajectory on hazardous terrain is shown in Fig. 2. In this scenario, we assume the rover gets the required initial hopping velocity through its internal

actuators, such as the flywheel, which has already been investigated in some research (Allen et al., 2013; Hockman et al., 2017). Under the action of initial velocity, the rover performs orbital motion without external control force. In this paper, the initial velocity is executed for each single hop, and it is assumed that the rover approximately stops at the landing point by grabbing mechanism or pulse maneuver to avoid possible rebound and sliding. The abilities to start hopping by internal actuators and stop at the landing point for each single hop are the limitations of this paper. Due to the relatively short distance of each single hop, the generally small size of the hopping rover, and limited configuration capabilities (Allen et al., 2013; Hockman et al., 2017), using internal actuators to get the initial velocity is more feasible than using thrusters. Therefore, the optimization of the hopping trajectory in this case is to design the initial velocity.

Some studies have also considered using a collision contact model to gain the take-off velocity (Liu et al., 2017), thereby realizing multiple consecutive hops. However, this method may cause a large position error because of the influence of the rover's configuration and motion attitude, as well as the uncertainty of complex terrain. Dividing these consecutive hops into independent single hops for which the rover stops at the landing point can get relatively better position precision. Thanks to the hopping mode, the rover can jump over a small terrain zone with a single hop. If the terrain zone cannot be jumped in a single hop with certain constraints, such as the hopping velocity not exceeding the maximum available velocity and the escape velocity on the surface, detours and multiple hops must be used to bypass it. Therefore, the hopping trajectory needs to be designed considering both the distribution of terrain obstacles and hopping peculiarities. In addition, the topic of this paper is the design of hopping trajectories, so we have not considered the shape and attitude information of the hopping rover.

2.2 Dynamic models

The motion of a hopping rover on a small body can be described in different coordinate frames. This paper mainly introduces the body-fixed frame O_f-$X_f Y_f Z_f$ and the local frame O_s-$X_s Y_s Z_s$. As shown in Fig. 3, where the small body is 433 Eros, the origin of the body-fixed frame is the mass center. The Z_f axis is the maximum moment of inertia axis of the target body, that is, the spin axis, and the X_f axis is the minimum moment of inertia axis. Y_f axis follows the right-hand rule. The origin of the local frame is located at the start point of the hopping motion. The $X_s Y_s$ plane is parallel to the local approximate plane, which is determined later, and the projection of the direction vector from start point

158 to end point on the $X_s Y_s$ plane is the positive X_s axis. The positive direction of the Z_s axis is the outward
159 normal direction of the $X_s Y_s$ plane, and the Y_s axis follows the right-hand rule.

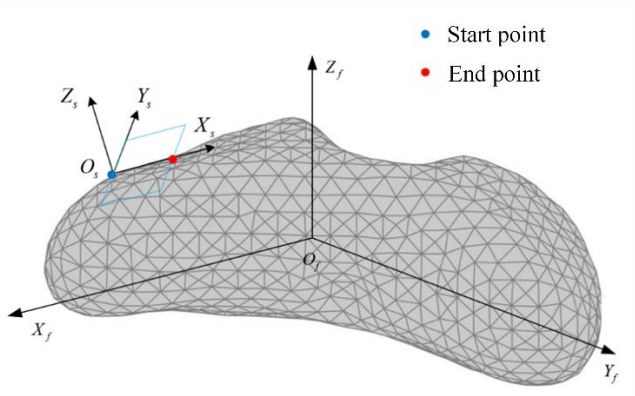

160
161 Fig. 3. The reference coordinate frames

162 When describing the dynamics of a hopping rover near the surface, it is generally assumed that the
163 small body rotates at a constant angular velocity around its main inertial axis Z_f, then the orbital dynamics
164 equation in the body-fixed frame is

165
$$\begin{cases} \dot{\boldsymbol{r}}_f = \boldsymbol{v}_f \\ \dot{\boldsymbol{v}}_f = -2\boldsymbol{\omega} \times \boldsymbol{v}_f - \boldsymbol{\omega} \times (\boldsymbol{\omega} \times \boldsymbol{r}_f) + \boldsymbol{g} \end{cases} \tag{1}$$

166 Where $\boldsymbol{r}_f$ is the rover's position vector in the body-fixed frame, $\boldsymbol{v}_f$ is the rover's velocity vector in the
167 body-fixed frame, $\boldsymbol{\omega}$ is the spin angular velocity vector of the small body, and $\boldsymbol{g}$ is the gravitational
168 acceleration vector.

169 To facilitate the following research, it is necessary to define the motion equation in the local frame.
170 The coordinate relationship of rover's position and velocity between the body-fixed frame and the local
171 frame is as follows

172
$$\begin{cases} \boldsymbol{r}_f = C_s^f \boldsymbol{r}_s + l \\ \boldsymbol{v}_f = C_s^f \boldsymbol{v}_s \end{cases} \tag{2}$$

173 Where $\boldsymbol{r}_s$ is the rover's position vector in the local frame, $\boldsymbol{v}_s$ is the rover's velocity vector in the local
174 frame, C_s^f is the coordinate transformation matrix from the local frame to the body-fixed frame, and l is
175 the position vector from the origin of the body-fixed frame to the origin of the local frame. From Eq. (1)
176 and (2), the orbit dynamics equation in the local frame is

177
$$\begin{cases} \dot{\boldsymbol{r}}_s = \boldsymbol{v}_s \\ \dot{\boldsymbol{v}}_s = -2(C_s^f)^{-1}(\boldsymbol{\omega} \times C_s^f \boldsymbol{v}_s) - (C_s^f)^{-1}\{\boldsymbol{\omega} \times [\boldsymbol{\omega} \times (C_s^f \boldsymbol{r}_s + l)]\} + (C_s^f)^{-1}\boldsymbol{g} \end{cases} \tag{3}$$

The study of surface hopping motion requires an accurate gravitational field model. The traditional spherical harmonic function and ellipsoidal harmonic function methods are not suitable because their results cannot converge near the surface of small bodies. In this paper, the polyhedron method (Werner and Scheeres, 1996) is used, and the gravitational acceleration is calculated by the following formula,

$$\boldsymbol{g} = -G\rho\left(\sum_{e\in \text{faces}} \boldsymbol{E}_e \cdot \boldsymbol{r}_e \cdot L_e - \sum_{f\in \text{faces}} \boldsymbol{F}_f \cdot \boldsymbol{r}_f \cdot \omega_f\right) \tag{4}$$

where G denotes the universal gravitational constant, ρ represents the density of the primary body, $\boldsymbol{r}_f$ and $\boldsymbol{r}_e$ represent the vectors from the field point to any arbitrary point on face f and edge e, respectively. $\boldsymbol{E}_e$ denotes the 3×3 dyad matrix defined as a function of the two meeting faces associated with edge e, and the 3×3 face dyad matrix $\boldsymbol{F}_f$ represents the outer product of normal vector of face f. Moreover, ω_f defines the signed solid angle of face f generated by the vectors from the field point to its vertexes and L_e represents a dimensionless logarithmic integration factor between the field point and edge e.

2.3 Safe hopping motion with uncertainties

Rock blocks, gravel piles, and pits of different sizes are distributed on the small body surface. This complex topographic condition poses a certain threat to the surface exploration rover. In this paper, these blocks, gravel piles, and pits over a certain size are regarded as terrain obstacles. For the identified pit obstacles, the rover will hop over them or bypass them, and the case that the rover goes into the pit and jumps out of it will not be considered. What's more, the hopping motion is designed to avoid a possible impact with the identified raised obstacle. If the rover is close to the raised obstacle during the hopping process, these obstacles are defined as hazard terrain. The more complex case that considers the shadow of a large boulder and surface properties will be studied in future work.

The relative position between the rover and the hazard terrain zone is usually used to assess the terrain threat and describe the safety of motion. This method is completely based on the rover's nominal state and does not consider the influence of uncertainties, so it is called the deterministic method. However, there are large uncertainties and disturbances in the surface dynamic environment of small bodies, and the estimated rover's states may have large deviations. Therefore, the deterministic method has certain limitations and low reliability when there are strong uncertainties. When the rover jumps over or passes by a hazard terrain zone by hopping, there are some uncertainties in the hopping trajectory due

205 to the influence of initial state errors and parameter uncertainties in the dynamic model. If the position
206 uncertainties are large, the rover may collide with or be very close to a hazard zone, even if the rover's
207 nominal trajectory is outside and keeps a certain distance from the hazard zone. Therefore, it is necessary
208 to consider the uncertainties during hopping trajectory design in order to improve both the accuracy of
209 motion and the reliability of safety assessment on hazardous terrain.

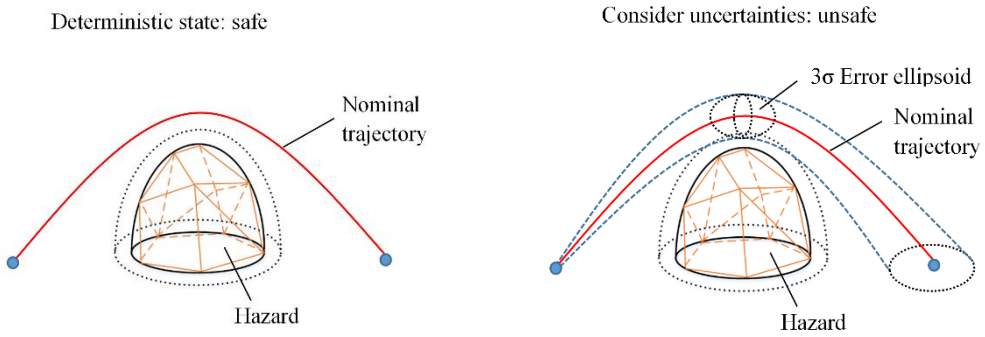

(a) (b)

210 Fig. 4. Description of safe hopping motion with uncertainties

211 The rover's state estimation errors can be described as having a Gaussian distribution. From the
212 rover's position mean and error covariance matrix, a 3σ error ellipsoid describing the position
213 uncertainties can be calculated. In terms of probability, the relationship between the 3σ ellipsoid and the
214 hazard zone is critical in describing the safety of hopping motion. As shown in Fig. 4 (a), the designed
215 nominal trajectory does not intersect with the hazard zone in the deterministic state, and the motion is
216 safe in this case. However, as shown in Fig. 4 (b), when errors and uncertainties are considered, the 3σ
217 error ellipsoid intersects with the hazard zone at a certain moment. The collision possibility between the
218 rover and the hazard zone will increase rapidly with the addition of the intersection part, which poses a
219 threat to the rover. In this case, the motion is unsafe. Therefore, the safety description that do not consider
220 uncertainties may be unreliable when position uncertainties are large. However, both cases are safe if the
221 nominal hopping trajectory is far from the hazard zone and the 3σ error ellipsoid is guaranteed to not
222 intersect with the hazard zone.

223 In this paper, we use a 3D topographic model with random terrain obstacles to simulate the complex
224 surface terrain. It is a limitation for current research since the actual complex surface terrain of a small
225 body could only be obtained after in-orbit observation. Each hazard terrain is represented by its smallest
226 circumscribed semi-ellipsoid (solid semi-ellipsoid in Fig. 4). Due to topographic uncertainties, the

location and size of the hazard zone may also be uncertain. To describe these uncertainties, the safety margin is added to the three semi-major axes of the semi-ellipsoid. Consequently, a reference closed semi-ellipsoid is defined to represent the hazard terrain (dotted semi-ellipsoid in Fig. 4). Therefore, the goal of safe hopping is to prevent the 3σ error ellipsoid from intersecting the reference closed semi-ellipsoid.

3 Hopping trajectory design

A variety of path planning methods have been applied to surface exploration rovers, but most of them plan the motion route (Kim et al., 2016; Ushijima et al., 2017; Jiang et al., 2020). In this paper, considering the peculiarity of hopping, the optimization of the trajectory on hazardous terrain is transformed into sequence path points planning and optimal hopping trajectory design. Trajectory planning directly on the 3D terrain is relatively difficult. In this paper, the 3D hazardous terrain feature is represented on a plane. Both motion paths and path points are planned on this plane. Two representative classical path planning methods, A* representing search-based path finding and RRT* representing sampling-based path finding, are used to get the optimal motion path. The sequence path points are planned based on hopping ability and terrain constraints. Considering the influence of initial state errors and parameter uncertainties, an optimal single hopping trajectory is designed between two adjacent path points, and then a continuous hopping trajectory of sequence path points can be developed.

3.1 Feasible path point zone

In this section, the local approximate plane is determined, and the terrain threat is presented on this plane. Then, the terrain obstacle is characterized and classified by the hopping ability. Finally, the feasible path point zone is determined. According to the 3D terrain elevation data of the hopping motion area, the surface terrain can be represented as raised obstacles and pits distributed on the plane. The terrain is identified by the least square median method. This algorithm mainly includes two tasks: fitting a local approximate plane, that is, determining the plane equation, and recognizing different terrain obstacles. The schematic diagram of the terrain identification principle is shown in Fig. 5.

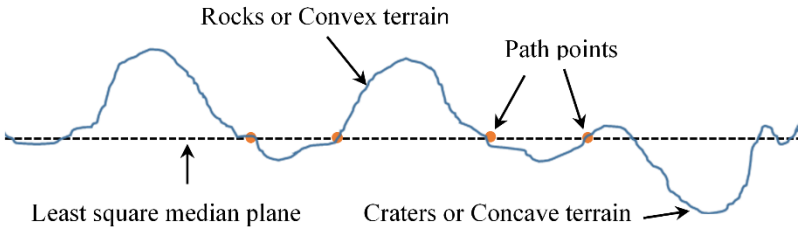

252

253 Fig. 5. Schematic diagram of the terrain identification

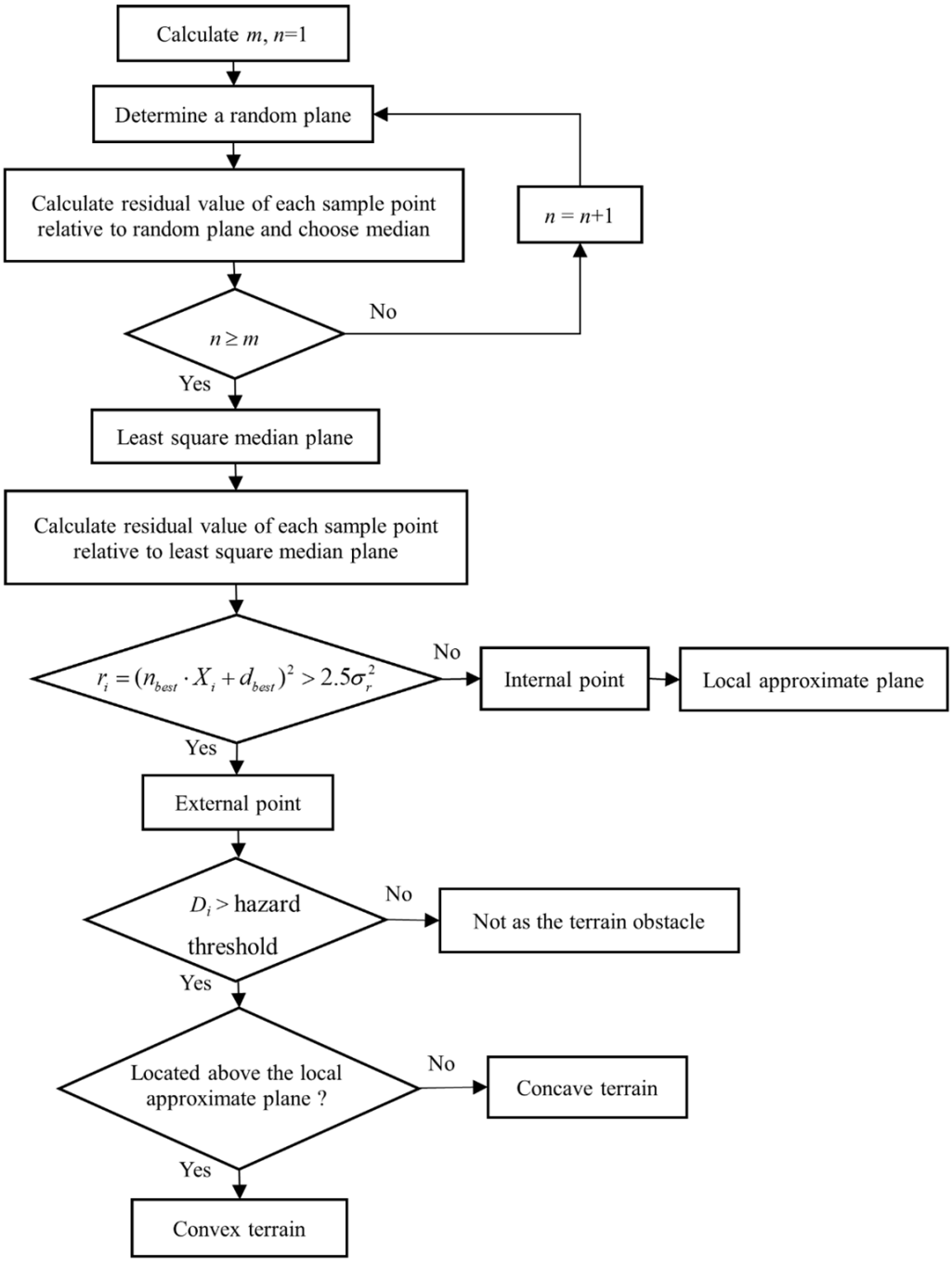

254

255 Fig. 6. Flow chart of least square median method

The algorithm flow chart is shown in Fig. 6. Three non-collinear points (x_a, x_b, x_c) are randomly selected from *N* sample points of surface terrain, and the equation $n \cdot X + d = 0$ of a random plane is determined, where *n* represents the plane normal vector and $n = (x_b - x_a) \times (x_c - x_a)$, $d = -n \cdot x_a$. The residual value $r_i = (n \cdot x_i + d)^2$ of each sample point x_i relative to this plane is calculated, and the median value of obtained r_i is chosen. Repeat the foregoing procedure $m = \ln(1-P) / \ln(1-(1-o)^3)$ times, where P is the expected probability and o is the statistic of the percentage of out-of-plane points to the total points. The corresponding plane of $r_{\min}$ which is the minimum value of the obtained *m* medians is recorded as the least square median plane.

The residual value of each sample point relative to the least square median plane is calculated. If it satisfies $r_i = (n_{best} \cdot X_i + d_{best})^2 > 2.5\sigma_r^2$, where $\sigma_r^2 = \left(1.4826\left(1+5/\left(N-3\right)\right)\right)^2 r_{\min}$, this sample point is an external point, otherwise, this sample point is an internal point. The plane of internal points is determined as the local approximate plane using the least square method. The point whose distance from the local approximate plane D_i is greater than the set hazard threshold is the terrain obstacle. The obstacle above the plane is a convex hazard, such as rocks or gravel piles. Otherwise, it is a concave low-lying obstacle, such as craters. In this way, the position and height (or depth) of terrain obstacles can be obtained using the above algorithm.

The terrain area is represented on the local approximate plane by a minimum circumscribed circle of terrain obstacle. Meanwhile, considering the terrain uncertainties, a margin value is added to the radius of the minimum circumscribed circle. The radius of the circle representing the *k*-th terrain obstacle can be expressed as

$$R_{ck} = R_k + \Delta_k, k = 1, 2, ..., Q \tag{5}$$

Where, Q represents the number of terrain obstacles, R_k represents the minimum circumscribed circle radius, and Δ_k represents the margin value of the *k*-th terrain obstacle. With the maximum height $h_{\max}$ that the hopping rover can jump over and the maximum distance $d_{\max}$ that can be reached in a single hop, which indicate the rover's hopping ability with velocity constraints, the terrain zone can be divided into two categories according to the height and plane size of obstacles

$$\begin{cases} \text{Jumpable zone,} & D_k < \gamma d_{\max} \cap H_k < \varepsilon h_{\max} \\ \text{Non-jumpable zone,} & D_k \geq \gamma d_{\max} \cup H_k \geq \varepsilon h_{\max} \end{cases}, k = 1, 2, ..., Q \tag{6}$$

Where, D_k is the diameter of the circle corresponding to the *k*-th terrain obstacle, and H_k is the height of the *k*-th terrain obstacle. γ and ε represent the weight coefficient. Thus, a plane with topographic feature information is available, and the plane area outside the circles is the feasible path points zone. On this plane, the traditional path planning algorithm can be used to plan the optimal path, and the sequence path points are determined on the feasible path points zone. During path planning on the plane, the path can pass through the jumpable area, but cannot pass through the non-jumpable area. With the relationship between the plane and 3D terrain, the determined sequence path points can be mapped to the 3D surface. The design of the optimal hopping trajectory is carried out based on three-dimensional path points.

3.2 Path points planning

In this section, the traditional path planning algorithm is used to acquire the optimal path between the start point and the end point, and the sequence path points are planned based on hopping peculiarities. The A* and RRT* algorithms are graph-search-based and random-sampling-based path planning methods, respectively, and both can be applied to the terrain plane determined in Section 3.1. In general, the A* algorithm can directly obtain the local optimal path. The RRT* is an improved method of the RRT algorithm, and it can obtain the optimal or asymptotically optimal path through continuous iteration.

3.2.1 A-based planning*

The A* algorithm is a direct search method for finding the shortest feasible path in a static grid graph. It is widely used in plane path planning problems because it is simple to implement and can ensure completeness and optimality. At the same time, it is also a heuristic search method that can design a heuristic function to find the optimal path. An evaluation function $F(n)$ is used for each traversed node to calculate the cost of passing the node. The general evaluation function is defined as

$$F(n) = G(n) + H(n) \tag{7}$$

Where, $H(n)$ represents the estimated cost from current node n to target point, that is, the designed heuristic function. In this paper, it is designed as the Manhattan distance. $G(n)$ calculates the motion cost from the start point to current node n.

The optimal path obtained by the traditional A* algorithm may have multiple turns in a short distance, which is an inherent path feature caused by the fact that the A* algorithm selects the node with the smallest $F(n)$ in each search. This local path situation need to be improved, and the basic principles

311 are as follows: the path does not pass through the non-jumpable area, the turn times are minimized, and
312 the path length is kept unchanged or is shortened according to the peculiarity that a hopping rover can
313 change the motion direction arbitrarily at the beginning of each hop.

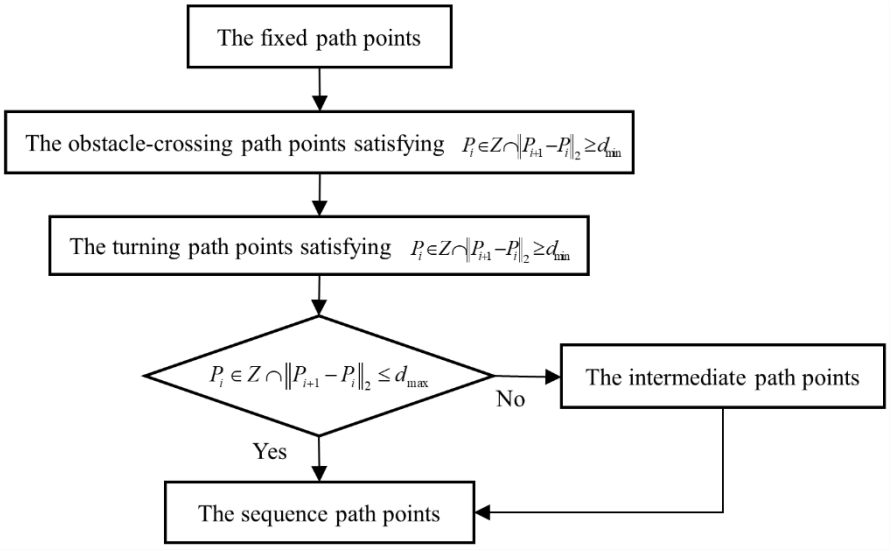

314

315 Fig. 7. Diagram of the sequence path points determination strategy for search-based path finding

316 The main purpose of path planning is to determine the sequence path points for hopping motion.
317 After the optimal path is planned, the sequence path points can be chosen from all nodes on the optimal
318 path. The sequence path points determination strategy for the search-based path finding algorithm is
319 given. Firstly, it is the fixed path point that includes both the start and end points. Secondly, it is the
320 obstacle-crossing path point. When the optimal path passes through the jumpable obstacle area, the two
321 closest nodes outside this area are selected as obstacle-crossing path points and simultaneously ensure
322 that the determined path points meet the requirement

323 $$P_i \in Z \cap \left\| P_{i+1} - P_i \right\|_2 \geq d_{\min}, i = 1, 2, \cdots n. \tag{8}$$

324 where, P_i represents the *i*-th path point, *Z* represents the feasible path points zone, and *n* represents the
325 number of path points. $d_{\min}$ represents the shortest distance of a single hop, which meets the requirement
326 $2d_{\min} \leq d_{\max}$. When the fixed path point is close to the terrain obstacle, the obstacle-crossing path point
327 may coincide with the fixed path point. That is, the fixed path point becomes the obstacle-crossing path
328 point. Then, it is the turning path point. The turning path point can be selected from the out-circle turning
329 nodes on the optimal path, and the determined path points also meet equation (8). The last is the
330 intermediate path point. If the distance between two adjacent determined path points is greater than $d_{\max}$,
331 the intermediate path point is added. The selection of intermediate path points is based on the multiple

identical hop strategy in Ref. Upadhyay and Aguiar (2019), and the number of intermediate path points to be added is determined by $d_{\max}$. The four types of path points above form the sequence path points from the start point to the end point. The schematic diagram of this process is shown in Fig. 7.

3.2.2 RRT-based planning*

The RRT algorithm has strong search ability and does not need to rasterize the search space. It is suitable for path planning in complex terrain environments. However, due to the uniform random sampling in the state space, its search time is long, and the generated path may not be optimal. The basic structure of the RRT* algorithm is similar to that of RRT, but RRT* adds the calculation process of parent node reselection and pruning to ensure the optimal solution (Karaman and Frazzoli, 2011). Before the preset maximum number of iterations is reached, RRT* will continuously reconnect the tree in each iteration to minimize the current cost based on the newly added nodes and their nearby nodes. Thus, the optimal solution, or asymptotically optimal solution, is achieved. After a feasible solution is found, the expansion process does not stop but continues to iterate to find a better solution. As the number of iterations increases, the result of RRT* will continue to approach the optimal solution.

When applying the RRT*, the algorithm needs to be constrained according to the hopping ability. The generation step size of a random tree and the search radius of a pruning operation can be set according to the maximum distance of a single hop. When generating the random tree, the sampling points can be in the jumpable area but cannot be in the non-jumpable area. After the approximate optimal solution is obtained, the determined nodes can be directly used as the sequence path points, but the path points need to satisfy the following constraint

$$P_i \in Z \cap d_{\min} \le \left\| P_{i+1} - P_i \right\|_2 \le d_{\max}, i = 1, 2, \cdots n. \tag{9}$$

All path points determined by RRT* can also be divided into the above four categories. Through the above constraint, the approximate optimal path that is suitable for hopping motion can be obtained by continuous iterative operation. Since RRT* is a random sampling algorithm, the generated optimal path has a certain randomness. That is, the optimal path of each plan may be different.

3.3 Optimal hopping trajectory

After determining the path points, the hopping trajectory between two adjacent points can be

calculated by solving the Lambert orbital boundary value problem in the irregular gravity field (Kalita and Thangavelautham, 2019). However, hopping motion has a certain instability, and it is easily affected by parameter uncertainties and initial state errors. Therefore, the actual hopping trajectory may deviate from the ideal nominal trajectory, thus affecting the end position precision of a single hop. In this section, the errors and uncertainties are modeled in the local frame, and the linear covariance method is used to quantitatively describe the influence of random variables. The performance index of a single hopping trajectory is given based on the established error covariance matrix. This index is minimized to obtain the optimal single hopping trajectory, and then the continuous hopping trajectory of sequence path points can be designed.

Firstly, the sequence path points planned on the topographic plane are projected onto its 3D topographic map to get the corresponding 3D path points. For a single hop of two adjacent path points on 3D terrain, the orbital dynamics equation in the local frame can be expressed as the functional form of the initial state and parameters, namely,

$$\boldsymbol{x}(t) = F\left(\boldsymbol{x}_0, \boldsymbol{\omega}, \boldsymbol{g}\right) \tag{10}$$

where $\boldsymbol{x}(t)$ represents the state vector at time t and $\boldsymbol{x}_0 = [\boldsymbol{r}_0, \boldsymbol{v}_0]$ represents the initial state vector. The uncertainty of each parameter in this formula will affect the state of rover. Among them, the initial state uncertainties reflect the influence of initial state errors, and the uncertainties of parameters $\boldsymbol{\omega}$ and $\boldsymbol{g}$ reflect the influence of dynamic model uncertainties. With Taylor series expansion, we can get

$$\delta \boldsymbol{x}(t) = \frac{\partial \boldsymbol{x}}{\partial \boldsymbol{x}_0}\delta \boldsymbol{x}_0 + \frac{\partial \boldsymbol{x}}{\partial \boldsymbol{\omega}}\delta \boldsymbol{\omega} + \frac{\partial \boldsymbol{x}}{\partial \boldsymbol{g}}\delta \boldsymbol{g} \tag{11}$$

The partial derivative in the above formula is the sensitivity matrix of each parameter, which can be obtained by the sensitivity analysis method (Montenbruck and Gill, 2000).

The dynamic equation can also be expressed as the state equation,

$$\dot{\boldsymbol{x}}(t) = f\left(\boldsymbol{x}_0, \boldsymbol{\omega}, \boldsymbol{g}\right) \tag{12}$$

The sensitivity matrix for any parameter can be expressed as $S_{\alpha}(t) = \left.\frac{\partial \boldsymbol{x}}{\partial \boldsymbol{\alpha}}\right|_t$, and it satisfies

$$\frac{\mathrm{d}S_{\alpha}(t)}{\mathrm{d}t} = \frac{\mathrm{d}\frac{\partial \boldsymbol{x}}{\partial \boldsymbol{\alpha}}}{\mathrm{d}t} = \frac{\partial \dot{\boldsymbol{x}}}{\partial \boldsymbol{\alpha}} + \frac{\partial \dot{\boldsymbol{x}}}{\partial \boldsymbol{x}}\frac{\partial \boldsymbol{x}}{\partial \boldsymbol{\alpha}} = \frac{\partial \dot{\boldsymbol{x}}}{\partial \boldsymbol{\alpha}} + \frac{\partial \dot{\boldsymbol{x}}}{\partial \boldsymbol{x}}S_{\alpha}(t) \tag{13}$$

When $\boldsymbol{\alpha} = \boldsymbol{x}_0$, $S_{\alpha}(0) = \left.\frac{\partial \boldsymbol{x}}{\partial \boldsymbol{x}_0}\right|_0 = I_{6\times 6}$. When $\boldsymbol{\alpha}$ is other parameters, $S_{\alpha}(0) = 0$. The sensitivity matrix

of initial state $S_{\boldsymbol{x}_0}(t)=\phi(t,0)$ is the state transition matrix of this system and satisfies $S_{\boldsymbol{x}_0}(0)=\phi(0,0)=I_{6\times 6}$. The sensitivity matrix of each parameter can be solved by the above differential equation. Assuming that the initial state errors and parameter uncertainties conform to the Gaussian distribution with a zero mean, the linear covariance matrix of the terminal state can be calculated from the covariance information and sensitivity matrix

$$\operatorname{cov}(\boldsymbol{x}(t_f))=\phi(t_f,0)\cdot\operatorname{cov}(\boldsymbol{x}_0)\cdot\phi(t_f,0)^{\mathrm{T}}+\sum_{i=1}^{k}\left.\frac{\partial \boldsymbol{x}}{\partial \boldsymbol{\alpha}_i}\right|_{t_f}\cdot\operatorname{cov}(\boldsymbol{\alpha}_i)\cdot\left(\left.\frac{\partial \boldsymbol{x}}{\partial \boldsymbol{\alpha}_i}\right|_{t_f}\right)^{\mathrm{T}} \tag{14}$$

Where, $\phi(t_f,0)$ is the state transition matrix from initial time 0 to terminal time t_f, and $\boldsymbol{\alpha}_i=[\boldsymbol{\omega},\boldsymbol{g}]$. Equation (14) reflects the uncertainty of the terminal state.

The performance index is given as follows

$$J=c\cdot E(\boldsymbol{v}_0)+trace(C_{t_f}) \tag{15}$$

Where, c is the weight coefficient, $E(\boldsymbol{v}_0)$ represents the energy consumption to obtain initial velocity, and $C_{t_f}=\operatorname{cov}(\boldsymbol{r}_{t_f})$ represents the error covariance matrix of terminal position. By minimizing the performance index J, the optimal single hopping trajectory that comprehensively considers energy consumption and terminal position errors can be generated. That is, the initial velocity can be obtained to realize this optimal single hopping trajectory between two path points. The ellipsoid representing the position error propagation on the optimal trajectory is the smallest under this index, while energy consumption is optimized. Then, the continuous hopping trajectory of sequence path points consists of multiple optimal single hopping trajectories. Since the designed trajectory of each single hop is the optimal trajectory, the ellipsoid on that trajectory is also the smallest. Therefore, reducing the impact of uncertainties can improve the end position precision of hopping motion, while the smallest error ellipsoid can enhance the safety in a certain sense from the perspective of safety description.

In this section, the least square median method is used to obtain the local approximate plane which is then used to represent hazardous terrains. Then, the optimal paths are planned using the A* and RRT* algorithms, respectively, and sequence path points are selected using the given strategies. Finally, the optimal hopping trajectory is designed to realize continuous hopping motion.

4 Collision-probability-based hopping trajectory optimization

In general, the safety of a designed hopping trajectory can be assessed by the relative position of the hopping rover to the hazard terrain zone. However, when considering the effect of errors and uncertainties, this paper adopts the collision probability of the hopping rover relative to the hazard zone to describe the safety performance. Compared to methods that only use the relative position, it is a more accurate and reliable index because it exploits the information about state uncertainties.

4.1 Collision probability

In this paper, the collision probability is defined as the probability that the rover's actual position is in a hazard zone. To evaluate the collision probability, we assume that the rover's position errors satisfy the Gaussian distribution with a zero mean. The probability density distribution can be given based on the nominal position and its error covariance matrix. The probability density function of position $\boldsymbol{r}$ is

$$f(\boldsymbol{r}) = \frac{1}{\sqrt{(2\pi)^3 |C|}} e^{-\frac{1}{2}(\boldsymbol{r}-\bar{\boldsymbol{r}})^{\mathrm{T}} C^{-1} (\boldsymbol{r}-\bar{\boldsymbol{r}})} \tag{16}$$

where $\bar{\boldsymbol{r}}$ is the nominal position and C is the error covariance matrix of position $\boldsymbol{r}$. When calculating collision probabilities, C is approximated as a constant matrix. The collision probability at a certain moment can be calculated from the probability density distribution information. According to physical characteristics of hazard terrain, a zone to represent this hazard terrain can be established. The collision probability is the accumulation of the probability density function of $\boldsymbol{r}$ inside the hazard zone. It can be calculated by the following integral

$$P_c = \iiint_{\textit{hazard zone}} f(\boldsymbol{r}) \mathrm{d}x\mathrm{d}y\mathrm{d}z = \iiint_{\textit{hazard zone}} \frac{1}{\sqrt{(2\pi)^3 |C|}} e^{-\frac{1}{2}(\boldsymbol{r}-\bar{\boldsymbol{r}})^{\mathrm{T}} C^{-1} (\boldsymbol{r}-\bar{\boldsymbol{r}})} \mathrm{d}x\mathrm{d}y\mathrm{d}z \tag{17}$$

The integral region is a three-dimensional hazard terrain zone. Through calculating the collision probability, the threat of hazard terrain to a rover under uncertainties can be more accurately assessed. Instead of only using the distance to describe the threat, applying the collision probability, which includes the uncertainty information about position, in the design of an optimal hopping trajectory can enhance the safety of hopping motion on hazardous terrain.

The collision probability shown in equation (17) contains a volume integral calculation. To improve the computational efficiency of solving the trajectory optimization problem, the volume integral

436 operation in this equation is approximated. As mentioned in Ref. Yuan et al. (2018), the difference in
437 probability density among points inside the hazard zone is small compared to that between the point
438 inside the hazard zone and the point near the nominal position. Therefore, the rover's position probability
439 density is approximately regarded as an average distribution in the hazard zone, so equation (17) is
440 simplified and the integral operation is removed. The location and size of hazard terrain are described by
441 the center $\boldsymbol{r}_c = [x_c, y_c, z_c]$ of reference semi-ellipsoid and its three semi-axis lengths a, b, c . The
442 probability density of point $\boldsymbol{r}_c = [x_c, y_c, z_c]$ is used to represent the probability density of each point in
443 the hazard zone, so equation (17) is simplified as

444 $$P_c = V \frac{1}{\sqrt{(2\pi)^3 |C|}} e^{-\frac{1}{2}(\boldsymbol{r}_c - \bar{\boldsymbol{r}})^{\mathrm{T}} C^{-1} (\boldsymbol{r}_c - \bar{\boldsymbol{r}})} \tag{18}$$

445 Here, $V = 2\pi abc/3$ is the volume of hazard zone. When there are multiple hazards that may collide
446 with the rover on the given terrain, the collision probability P_{ct} is the sum of collision probability
447 between the rover and each hazard, that is

448 $$P_{ct} = \sum_{i=1}^{n} P_{ci}, \quad i = 1, 2, \cdots n \tag{19}$$

449 where *n* is the number of possible collision hazards.

450 *4.2 Trajectory optimization*

451 The hopping trajectory design in this paper is to design the initial velocity to conduct orbital motion
452 of two known path points. No orbital control is applied during hopping. Therefore, the method, that
453 calculates collision probability in real time on the trajectory and applies orbital control maneuvers to
454 realize safe motion when the collision probability is large, is not adopted. Taking Equation (19) as the
455 safety performance index, it is obvious that there must be a hopping trajectory whose safety assessment
456 is the best. That is, the maximum of P_{ct} calculated on this trajectory is the minimum value of all feasible
457 trajectories. However, only minimizing collision probability is not the focus of this study. If Equation
458 (19) is directly added to the performance index (15) for optimization operation, a hopping trajectory with
459 the best comprehensive performance can be obtained. Even if the maximum of P_{ct} on the optimal
460 trajectory is the best of all feasible trajectories under that index, this optimal collision probability may
461 still be large. In some ways, this cannot guarantee a safe hopping motion. Therefore, we need to separate
462 the collision-probability-based safety evaluation from the optimal design of the hopping trajectory. The

463 optimal hopping trajectory is first designed by the performance index (15). Then, the safety is evaluated
464 by calculating the collision probability between the rover and the hazard zone on this hopping trajectory.
465 The sum of collision probabilities between the rover and all possible collision hazards can be
466 calculated on the continuous hopping trajectory designed in Section 3.3. Generally, the closer the rover
467 is to the hazard on the trajectory, the greater the collision probability. For any single hopping trajectory,
468 the value P_{ct} is mainly contributed by the P_c of nearest hazard, and the value P_c calculated by other
469 hazards is relatively low at this moment. Therefore, the designed hopping trajectory needs to be far away
470 from the hazard zone to ensure the safety.
471 In this paper, the maximum threshold of P_{ct} is set to optimize the planning of sequence path points
472 so as to enhance the safety of motion. If P_{ct} exceeds the given threshold, the local path points are
473 replanned to optimize the sequence path points according to the path points decomposition and
474 replacement strategy. The optimized sequence path points are used to redesign the optimal single hopping
475 trajectory between two adjacent path points. Then, the collision-probability-based continuous optimal
476 hopping trajectory can be generated. Designing the optimal hopping trajectory based on the performance
477 index (15) and optimizing the continuous hopping trajectory based on the collision probability can not
478 only improve the end position precision as well as the energy consumption, but also enhance the safety
479 of hopping motion on hazardous terrain.
480 The path points decomposition and replacement optimization strategy based on collision probability
481 is given as follows
482 1) When P_{ct} is greater than the given threshold, the circle corresponding to the hazard which is
483 closest to the hopping trajectory is expanded, that is, the radius R_{cx} of this circle is increased. The
484 nominal position is $\bar{\boldsymbol{r}}_{\max}$ when P_{ct} gets the maximum value. The maximum collision probability of the
485 rover to the closest hazard at this position can be expressed as

486 $$P_{\mathrm{c}}^{\max} = V \frac{1}{\sqrt{(2\pi)^3 |C|}} e^{-\frac{1}{2}(\boldsymbol{r}_{\mathrm{c}} - \bar{\boldsymbol{r}}_{\max})^{\mathrm{T}} C^{-1} (\boldsymbol{r}_{\mathrm{c}} - \bar{\boldsymbol{r}}_{\max})} \tag{20}$$

487 By reducing $P_{\mathrm{c}}^{\max}$ to its λ times, $\lambda \in (0,1)$, and ensuring that the reduced P_{ct} is less than the
488 given threshold, the maximum collision probability of the nominal position $\bar{\boldsymbol{r}}_{\lambda}$ to the closest hazard at
489 this moment can be expressed as

$$\lambda P_{\mathrm{c}}^{\max} = V \frac{1}{\sqrt{(2\pi)^3 |C|}} e^{-\frac{1}{2}(\boldsymbol{r}_c - \bar{\boldsymbol{r}}_\lambda)^{\mathrm{T}} C^{-1} (\boldsymbol{r}_c - \bar{\boldsymbol{r}}_\lambda)} \tag{21}$$

Then $\bar{\boldsymbol{r}}_\lambda$ satisfies

$$(\boldsymbol{r}_c - \bar{\boldsymbol{r}}_\lambda)^{\mathrm{T}} C^{-1} (\boldsymbol{r}_c - \bar{\boldsymbol{r}}_\lambda) = 2 \ln \frac{V}{\lambda P_{\mathrm{c}}^{\max} \sqrt{(2\pi)^3 |C|}} \tag{22}$$

Therefore, the radius of the circle can be approximately increased by $\Delta R_{cx} = \left\| \bar{\boldsymbol{r}}_\lambda - \bar{\boldsymbol{r}}_{\max} \right\|_2$.

2) The enlarged circle is a new hazard zone, and the original path points in the new hazard zone are replaced by new path points. The new path point can be chosen from the edge of the extended circle. The new obstacle-crossing path point is determined based on the strategy in section 3.2.1 and can be adopted at the intersection between the edge of the extended circle and the planned path. If the distance between two new obstacle-crossing path points is greater than $d_{\max}$, this hazard cannot be passed by jumping and the path point decomposition strategy is applied to get one or more decomposed intermediate path points. Similar to the intermediate path points, the decomposed intermediate path points are also determined by a multiple identical hop strategy and are selected on the edge of the extended circle. The number of decomposed intermediate path points is determined by both $d_{\max}$ and P_{ct} after decomposition.

3) The sequence path points determination strategy in section 3.2.1 is used to determine the new turning path points and intermediate path points.

4) To sum up, with the fixed path points, the optimized sequence path points can be gained.

After the optimized sequence path points are obtained through the above strategies, the optimal single hopping trajectory needs to be redesigned. Theoretically, if there is no influence from errors and uncertainties, the rover can hop along with the designed path points. Even if the hopping trajectory is designed by minimizing the performance index (15), there may still be a small position error with the target path point during landing. When applied to actual cases, an optimal hopping trajectory between the start point and the next path point is first designed. Then, the rover moves toward the target at the designed initial velocity and stops on the surface through a landing mechanism. For the next hop, the actual landing point of the last hop is taken as the start point to design the optimal trajectory to the next target path point. Similarly, the rover moves toward the next target at the designed initial velocity until the end point becomes the next target path point. Since we have considered the safety performance in advance and have planned the optimal sequence path points, the optimal hopping trajectory can achieve

continuously safe and accurate motion on hazardous terrain according to the current start point and the next target path point for each hop.

In this section, the definition of collision probability is given, and then the collision probability is assessed on the predesigned optimal hopping trajectory. According to the set safety threshold, the hazard zone that has an unsafe collision probability can be identified. With the proposed decomposition and replacement optimization strategy, the corresponding unsafe path points can be optimized. Finally, the renewed hopping trajectory of optimized sequence path points is reliable.

5 Numerical simulations

In this section, the small body 433 Eros is taken as an example to simulate and verify the proposed method under the simulated surface hazardous terrain. The physical parameters of 433 Eros are: the three-dimensional size is 34.4 km× 11.2km × 11.2km, the mass is 6.69×10^{15}kg, the density is 2.67×10^{3}kg/m^3, the spin angular velocity around its inertial axis is 3.31×10^{-4}rad/s, and the gravitational constant is 6.67×10^{-11} Nm^2/kg^2. According to the data obtained from the NEAR mission, the surface of 433 Eros is covered with complex regolith, an abundance of ejecta blocks, and many craters of different sizes. Small craters are very rare compared to large craters over 30 meters in diameter. However, most blocks are down to a meter in size, and there are on average about 25 blocks larger than 8 m across per square kilometer based on the obtained data (Veverka et al., 2001).

From the data of the NEAR mission (Veverka et al., 2001), the local terrain is relatively flat within a certain scale for most areas on the surface if there are not large craters. Here, we assume that the least square median method can fit a local approximate plane for the chosen local terrain. In this part, two different simulation terrain models of 400m × 400m are used to describe the surface hazardous terrain. As shown in Fig. 8, the convex parts represent hazard terrains such as rocks, and the concave parts represent low-lying terrains such as craters. Fig. 9 is the topographic contour map corresponding to the two terrains.

The parameters of hopping ability are set to: $d_{\min}=10\text{m}$, $d_{\max}=60\text{m}$, and the weight coefficients γ and ε are set to 0.8. For the above 3D terrain scenes, the local approximate plane is determined, and the complex terrain is characterized. The simulation results are shown in Fig. 10. The circles are terrain obstacle areas, and other areas are the feasible path points zone. Dark gray areas are hazard terrain obstacles such as rocks, light gray areas are low-lying terrain obstacles such as craters, and other areas

are the approximately flat terrains. The circles with a black border are the non-jumpable zones, and other circles are the jumpable zones.

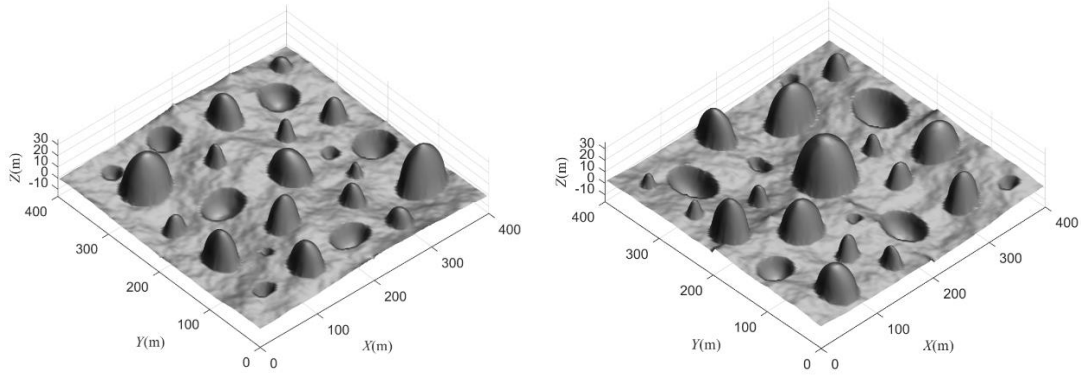

(a) Terrain A (b) Terrain B

Fig. 8. 3D terrain simulation map

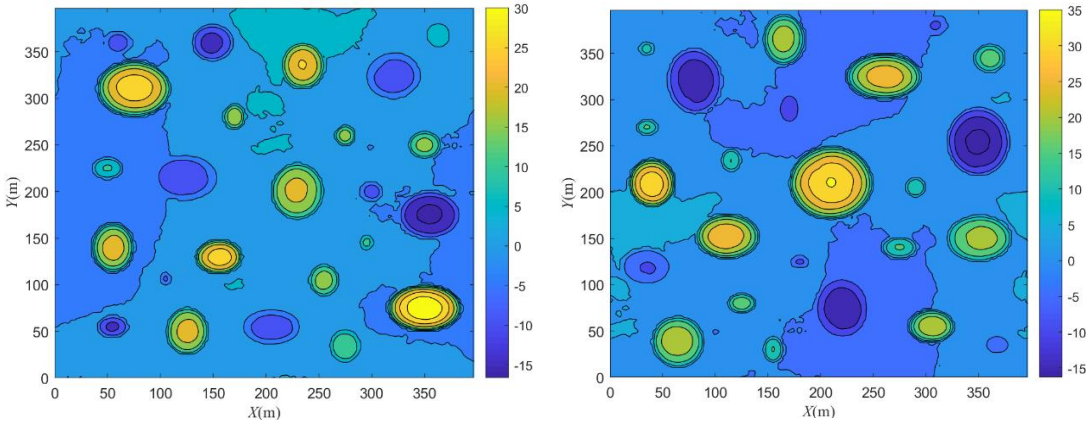

(a) Terrain A (b) Terrain B

Fig. 9. Topographic contour map

Table 1

Simulation parameters of path planning algorithm

Parameters	Start point(m)	End point(m)	Number of jumpable obstacles	Number of non-jumpable obstacles
Terrain A	[7.5,387.5]	[392.5,12.5]	12	12
Terrain B	[2.5,7.5]	[392.5,392.5]	12	12

The path planning algorithm is used to plan the optimal motion path on the local approximate plane after terrain characterization. The simulation parameters are shown in Table 1. The grid cell size of A* is set at 5m. For determining hopping path points with the optimal path of A*, the selectable point is the center or vertex of the grid. The rest parameters setting of RRT* are: the random tree growth step size is $S_{tree} = \kappa d_{\max}$, the search radius is $S_r = \beta d_{\max}$, and the number of random sample points is $N_{\text{samples}} = 4000$, where κ and β represent weight coefficients and are set to $\kappa = 0.9$ and $\beta = 0.8$

during simulation. The hopping path points on the optimal path of RRT* are directly determined by its nodes. The simulation results are shown in Figs. 11 and 12. The blue dotted line in Fig. 11 represents the local path improvement for the A* short-distance multiple turn problem. The solid black line in Fig. 12 represents the optimal or asymptotically optimal path of RRT*. Table 2 shows the number of planned sequence path points.

Table 2
The number of planned sequence path points

Based algorithm	A*	RRT*
Terrain A	17	15
Terrain B	21	14

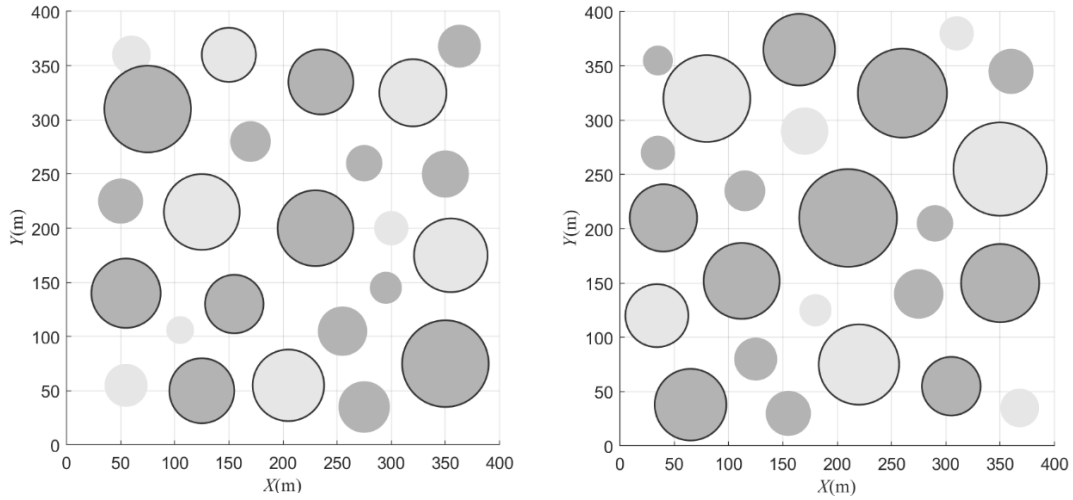

(a) Terrain A (b) Terrain B

Fig. 10. Topographic feature plane

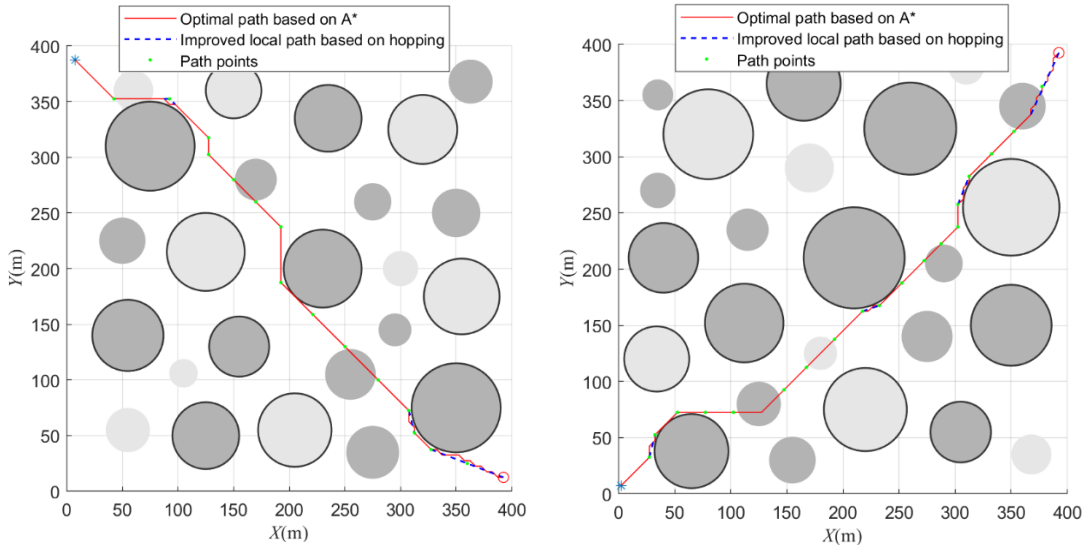

(a) Terrain A (b) Terrain B

Fig. 11. A* path planning and local improvement results

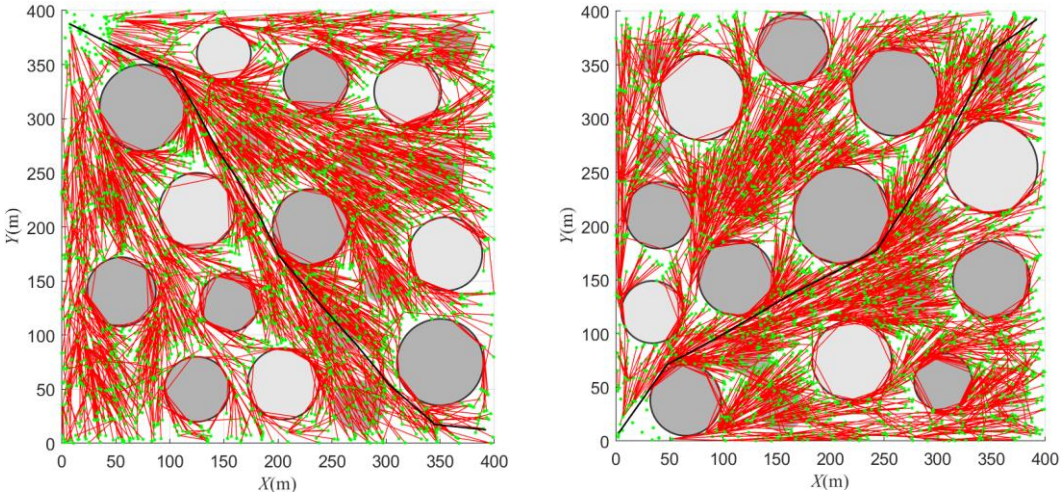

(a) Terrain A (b) Terrain B

Fig. 12. RRT* path planning results

With respect to the time consumption of these two methods, A* is fast because it searches the path toward the end point with an evaluation function, but RRT* takes more time since it is a random search method based on samples and it needs to iterate continuously to find the approximate optimal solution. As we can see from the results in Figs. 11 and 12, the planned path of A* can detour to pass big obstacles. The planned path of RRT* can also bypass big obstacles, but this path is a little straighter than that of A* since RRT* has the calculation of parent node reselection and pruning and iterates continuously to the optimal path. Meanwhile, the number of obtained path points for RRT* is less than that for A*, so the computing time for a continuous optimal hopping trajectory will also decrease for RRT*-based path points. The two types of methods have their own advantages and disadvantages, which can be selected according to the actual situation in the application.

The three-dimensional path points are reflected through the corresponding path points on the local approximate plane. Then, as is given in Section 3.3, the optimal single hopping trajectory between two adjacent path points is designed in 3D space, and then the continuous optimal hopping trajectory of sequence path points is obtained. The standard deviation of initial state errors and dynamic model parameter uncertainties are shown in Table 3. Here, we assume that standard deviation in three direction is the same for a state vector. In this section, two kinds of continuous hopping trajectories, the minimum-initial-velocity hopping trajectory [28] and the optimal hopping trajectory proposed in this paper, are designed based on the sequence path points planned by A* on terrain B, and there is an assumption that, for the design of a hopping trajectory, the gravity vector is nearly constant but may change with each single hop. Two kinds of trajectory on 3D terrain are shown in Fig. 13. Since the height of the minimum-

initial-velocity hopping trajectory is smaller than that of the optimal hopping trajectory, the collision probability of the minimum-initial-velocity hopping trajectory with hazard terrain is obviously larger than that of the optimal hopping trajectory. What's more, the minimum-initial-velocity hopping trajectory is even possible to pass through hazard terrain. From the 2000 Monte Carlo simulations shown in Fig. 14, the position error at the end point of the continuous hopping trajectory, which is composed of optimal single hops, is smaller than that of the minimum-initial-velocity continuous hopping trajectory.

Table 3

Uncertainty conditions of parameters

Parameters	Initial position	Initial velocity	Gravitational acceleration $\boldsymbol{g}$	Spin angular velocity $\boldsymbol{\omega}$
Standard deviation	0.1(m)	0.02(m/s)	1%(m/s^2)	10^{-5}%(rad/s)

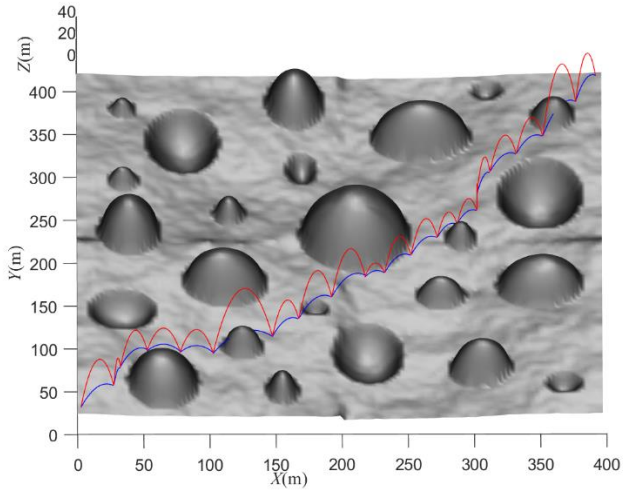

Fig. 13. Two hopping trajectories based on A* path points

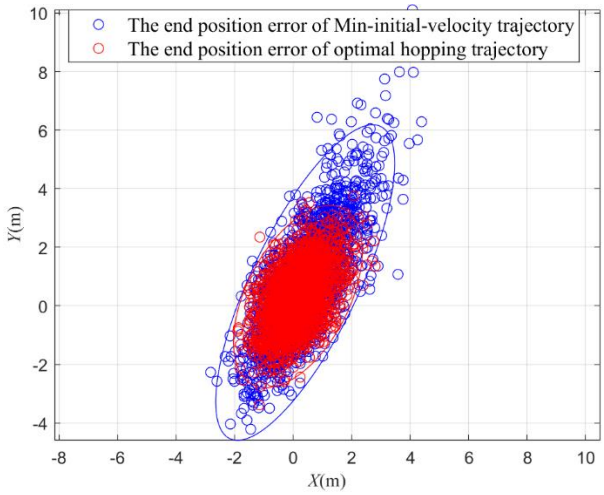

Fig. 14. Comparison of end position errors of two hopping trajectories

For the two simulated hazardous terrain scenarios, the A*-based path points optimization results are shown in Figs. 15 and 16, and the RRT*-based path points optimization results are shown in Figs. 18 and

19. The black dotted circles in the figures represent the corresponding hazard terrain to be expanded. The routes in Figs. 15(a), 16(a), 18(a), and 19(a) are the motion routes of sequence path points. For the RRT* algorithm, this motion route is the optimal path. Nevertheless, for the A* algorithm, this motion route is different from the planned optimal path. Table 4 shows the number of sequence path points after optimization. The routes in Figs. 15(b), 16(b), 18(b), and 19(b) are the motion routes of optimized sequence path points.

In this section, when calculating the collision probability, the standard deviation of position is set as a fixed value of 10m. The collision probability before optimization is shown as the blue curve in Figs. 17 and 20. According to the set collision probability threshold, the corresponding hazard terrain can be recognized when the collision probability is greater than the threshold. After the hazard zone is extended on the plane and the path points are replanned, the collision-probability-based optimized sequence path points are determined. For the optimized sequence path points, the hopping trajectory is redesigned in 3D space and the collision probability is calculated again. The collision probability after optimization is shown as the yellow curve in Figs. 17 and 20.

As shown in Fig. 21, the hopping trajectory on 3D hazardous terrain is designed with RRT*-based sequence path points. From the analysis of Figs. 20 and 21, although the hopping trajectory does not pass through the jumpable hazard zone for a single hop, there may be a large collision probability, so that it is still potentially risky. Fig. 22 shows the hopping trajectory on the 3D terrain after RRT*-based sequence path points optimization.

As can be seen from Figs. 15, 16, 18, and 19, when the collision probability is greater than the given threshold, the path points are optimized by increasing the distance between the path points and the hazard terrain or increasing the intermediate path points at the hazard terrain. It can be seen from Figs. 17 and 20 that the collision probability after optimization is significantly reduced where the collision probability is larger before optimization. From the comparison of Figs. 21 and 22, to enhance the safety of hopping motion, the distance between the hopping trajectory and the hazard terrain is increased through the optimization of path points, and the rover can bypass the potential hazard terrain by detouring.

For the application of the proposed method, time and certain software abilities are required for each step. It cannot be conducted directly on a hopping rover, which is always small and equipped with simple devices. However, it can be calculated on the orbiting spacecraft in advance and then send orders to the

hopping rover, which is already deployed on the target surface area of a small body. For the steps of determining a local plane and planning an optimal path, the computing time will depend on the complexity of the local terrain and the chosen path planning algorithm. Once path points are selected, the design of an optimal hopping trajectory and the optimization based on collision probability are fast because the hopping motion is ballistic.

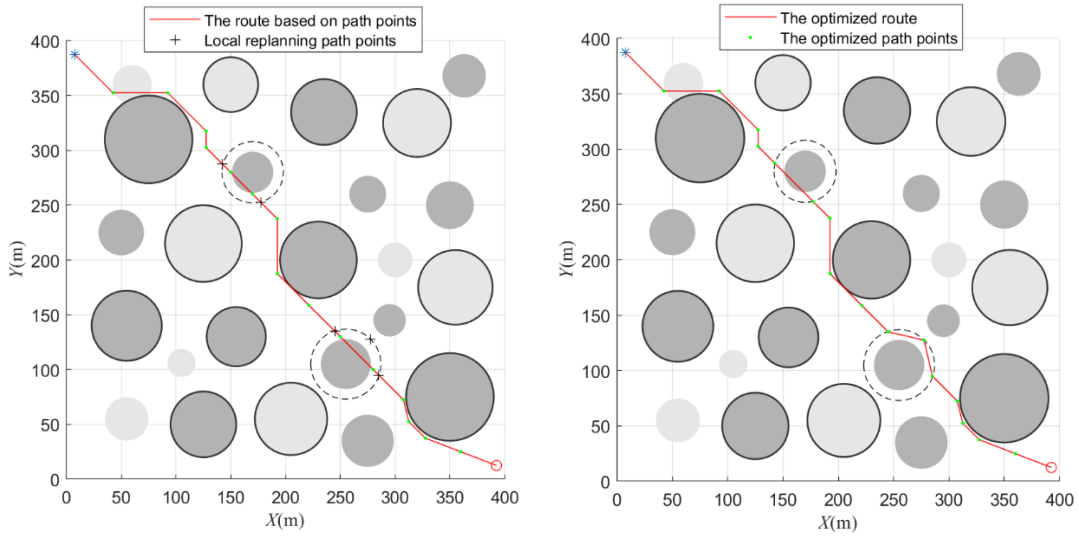

(a) Before optimization (b) After optimization

Fig. 15. A*-based sequence path points optimization on terrain A

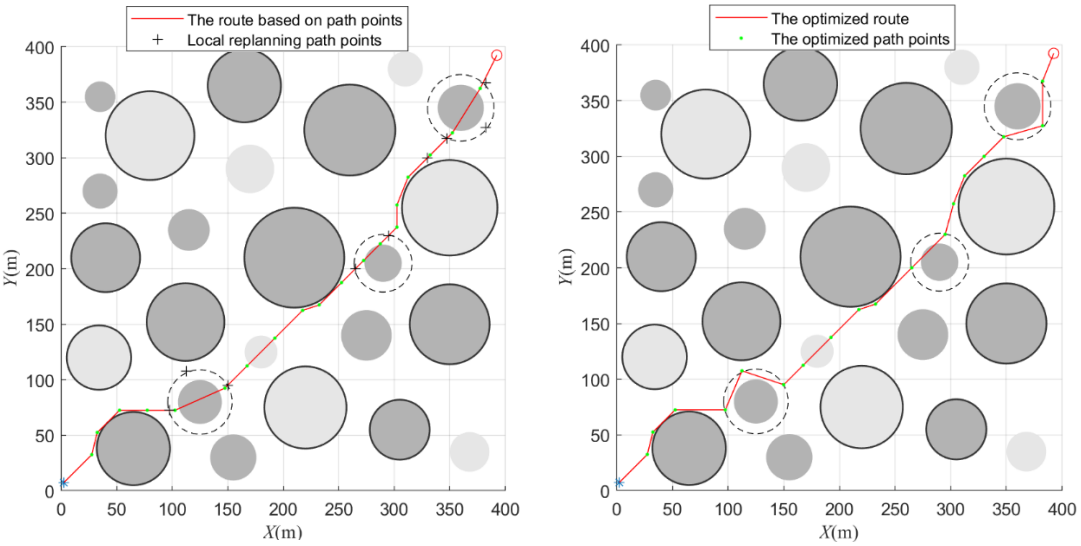

(a) Before optimization (b) After optimization

Fig. 16. A*-based sequence path points optimization on terrain B

Table 4

The number of sequence path points after optimization

Based algorithm	A*	RRT*
Terrain A	18	15
Terrain B	20	15

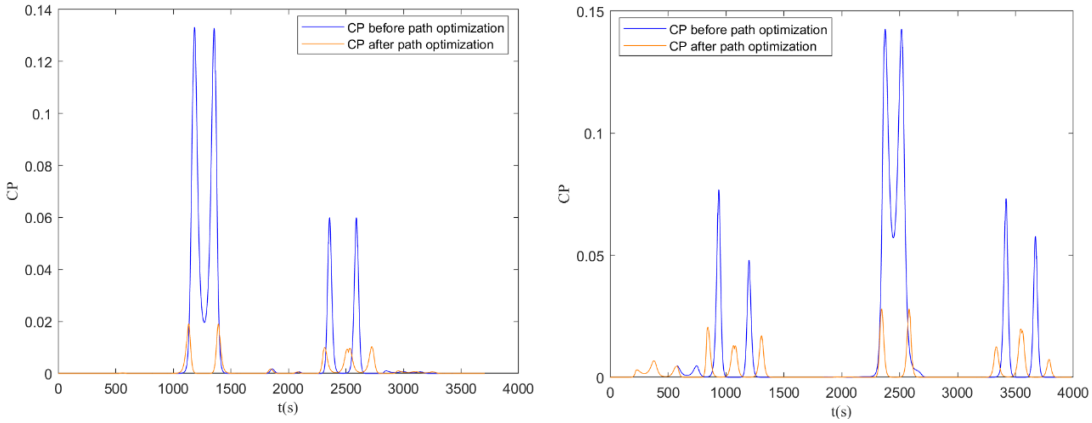

(a) Terrain A (b) Terrain B

632 Fig. 17. A*-based comparison of CP before and after optimization

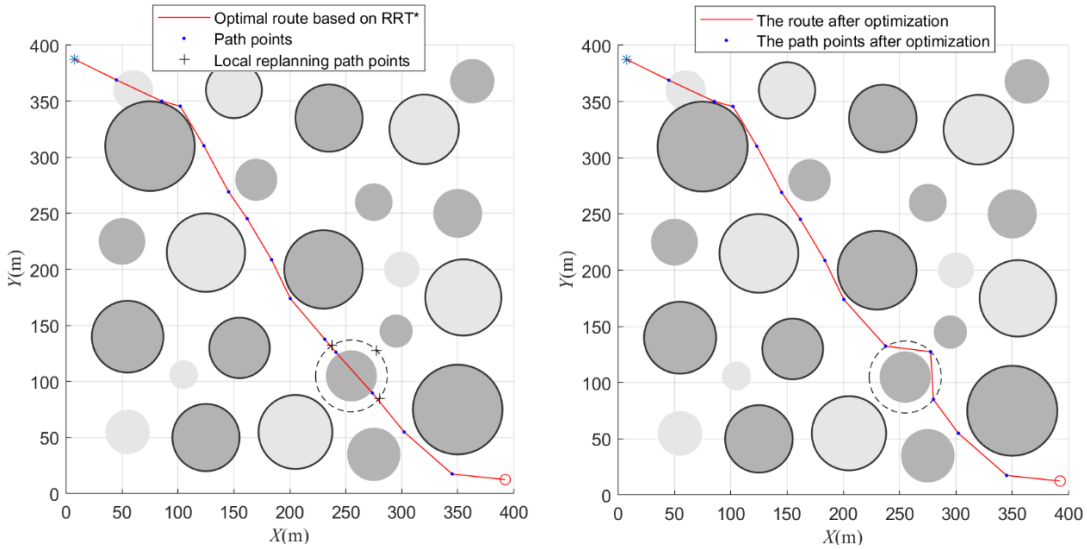

(a) Before optimization (b) After optimization

633 Fig. 18. RRT*-based sequence path points optimization on terrain A

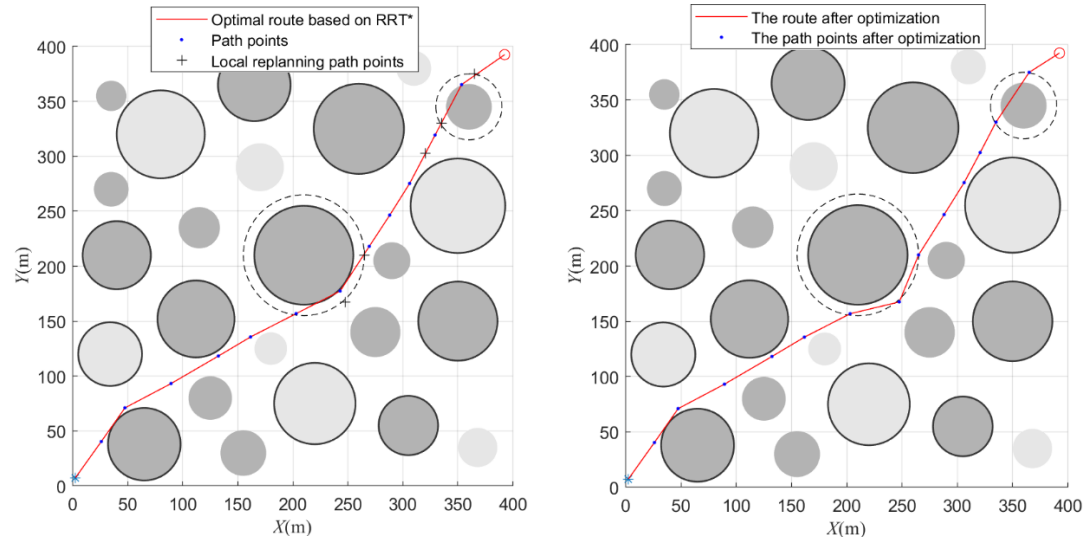

(a) Before optimization (b) After optimization

634 Fig. 19. RRT*-based sequence path points optimization on terrain B

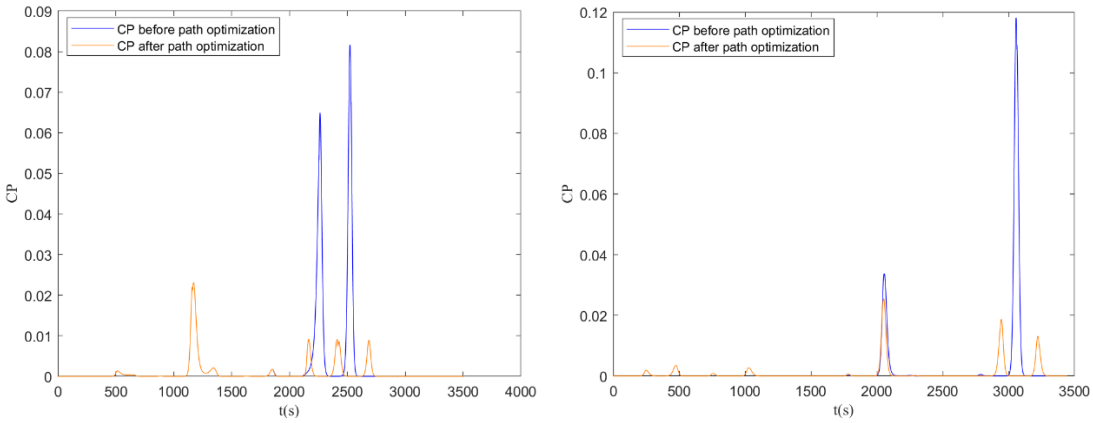

(a) Terrain A (b) Terrain B

635 Fig. 20. RRT*-based comparison of CP before and after optimization

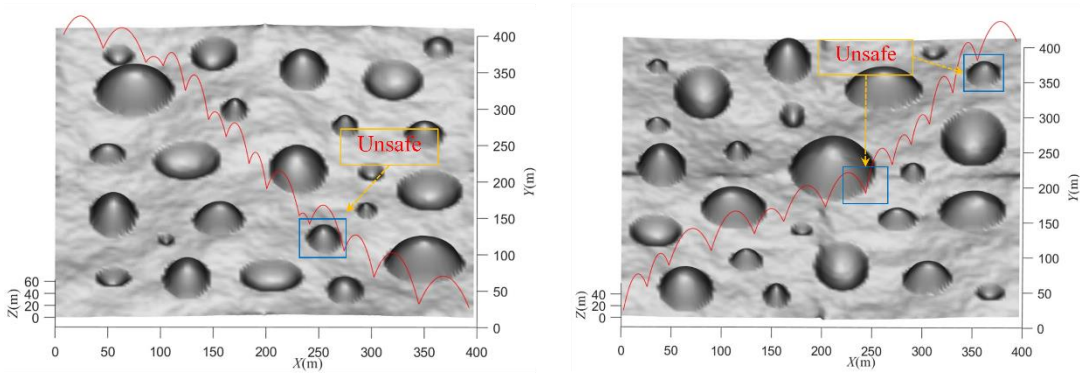

(a) Terrain A (b) Terrain B

636 Fig. 21. Hopping trajectory design of RRT*-based path points

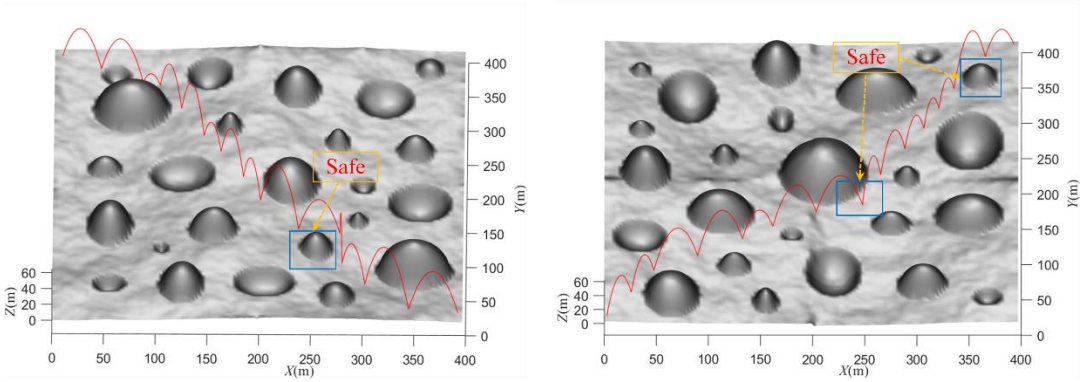

(a) Terrain A (b) Terrain B

637 Fig. 22. Optimized hopping trajectory of optimized RRT*-based path points

638 **6 Conclusion**

639 This paper proposes a hopping trajectory optimization method based on collision probability, which
640 can be used for the safe motion of a hopping rover on hazardous terrain. Firstly, the least square median
641 method is used to characterize surface hazardous terrain. It is possible to obtain a local approximate plane
642 with terrain feature information and the feasible path points zone for hopping. Secondly, two

representative classical path planning algorithms, A* and RRT*, are applied, and sequence path points are planned according to hopping peculiarities. Then, considering the effects of initial state errors and dynamic parameter uncertainties, the performance index is derived for the design of an optimal single hopping trajectory between two path points. Therefore, a continuous hopping trajectory can be generated. Finally, the local hopping trajectory that needs to be optimized is identified by calculating the collision probability, and the sequence path points are optimized through path point decomposition and replacement strategy. Consequently, the continuous optimal hopping trajectory is redesigned. It can be seen from simulation results that the collision probability on the optimized trajectory is significantly reduced, thus effectively enhancing the safety of hopping motion. The research content of this paper can provide a reference for future surface exploration missions of small bodies to conduct safe motion on hazardous terrain with a hopping rover.

Acknowledgments

This work was supported by the National Natural Science Foundation of China, No. 61973032.

References

Allen, R., Pavone, M., McQuin, C., et al., 2013. Internally-actuated rovers for all-access surface mobility: Theory and experimentation. In: IEEE International Conference on Robotics and Automation, Karlsruhe, Germany, pp.5481-5488.

Bellerose, J., Scheeres, D., 2008. Dynamics and control for surface exploration of small bodies. In: AIAA/AAS Astrodynamics Specialist Conference and Exhibit. https://doi.org/10.2514/6.2008-6251.

Berry, K., Sutter, B., May, A., et al., 2013. OSIRIS-REx touch-and-go (TAG) mission design and analysis. In: 36th Annual AAS Guidance and Control Conference.

Cui, P., Liu, Y., Yu, Z., et al., 2017. Intelligent landing strategy for the small bodies: from passive bounce to active trajectory control. Acta Astronaut. 137, 232–242. http://doi.org/10.1016/j.actaastro.2017.04.033.

Ge, D., Cui, P., and Zhu, S., 2019. Recent development of autonomous GNC technologies for small celestial body descent and landing. Prog. Aerosp. Sci. 110, 1-14. https://doi.org/10.1016/j.paerosci.2019.06.002

Hockman, B., Frick, A., Reid, R., et al., 2017. Design, Control, and Experimentation of Internally-Actuated Rovers for the Exploration of Low-gravity Planetary Bodies. J. Field Robot. 34 (1), 5-24. https://doi.org/10.1002/rob.21656.

671 Hockman, B., and Pavone, M., 2017. Stochastic motion planning for hopping rovers on small solar system bodies.
672 In: 18th International Symposium on Robotics Research, Puerto Varas, Chile.
673 https://doi:10.1007/978-3-030-28619-4_60.
674 Hockman, B., and Pavone, M., 2018. Traversability of Hopping Rovers on Small Solar System Bodies. In:
675 International Symposium on Artificial Intelligence, Robotics and Automation in Space, ESA, French Guiana,
676 pp. 1-8.
677 Hu, H., Zhu, S., and Cui, P., 2016. Desensitized optimal trajectory for landing on small bodies with reduced landing
678 error. Aerosp. Sci. Technol. 48, 178–185. https://doi.org/10.1016/j.ast.2015.11.006.
679 Jiang, J., Zeng, X., Guzzetti, D., and You, Y., 2020. Path planning for asteroid hopping rovers with pre-trained deep
680 reinforcement learning architectures, Acta Astronaut. 171, 265–279.
681 https://doi.org/10.1016/j.actaastro.2020.03.007.
682 Kalita, H., and Thangavelautham, J., 2019. Motion planning on an asteroid surface with irregular gravity fields, 42nd
683 AAS Rocky Mountain Section Guidance and Control Conference, Rocky Mtn Sect, Breckenridge, CO.
684 Karaman, S., and Frazzoli, E., 2011. Sampling-based algorithms for optimal motion planning, Int. J. Robot. Res. 30
685 (7), 846-894. https://doi.org/10.1177%2F0278364911406761.
686 Kim, K., Chen, L., Cera, B., et al., 2016. Hopping and rolling locomotion with spherical tensegrity robots. In:
687 IEEE/RSJ International Conference on Intelligent Robots and Systems, Daejeon, Korea.
688 https://doi.org/10.1109/IROS.2016.7759643.
689 Kubota, T., Yoshimitsu, T., 2013. Intelligent rover with hopping mechanism for asteroid exploration. In: 6th
690 International Conference on Recent Advances in Space Technologies (RAST), Istanbul, TURKEY, pp. 979-984.
691 Lange, C., Ho, T., Grimm, C., et al., 2018. Exploring small bodies: Nano- and micro-lander options derived from
692 the mobile asteroid surface scout. Adv. Space Res. 62, 2055–2083. https://doi.org/10.1016/j.asr.2018.05.013.
693 Li, X., Sanyal, A., Warier, R., Qiao, D., 2020. Landing of hopping rovers on Irregularly-shaped small bodies using
694 attitude control. Adv. Space Res. 65, 2674-2691. https://doi.org/10.1016/j.asr.2020.02.029.
695 Li, X., Scheeres, D., Qiao, D., 2022. Bouncing Return Trajectory Design for Precise Lander Deployment to Asteroids.
696 J. Guid. Control Dynam. 45 (1), 121-137. https://doi.org/10.2514/1.G006016.
697 Liu, X., Yang, H., and Li, S., 2021. Collision-Free Trajectory Design for Long-Distance Hopping Transfer on
698 Asteroid Surface Using Convex Optimization. IEEE Trans. Aerosp. Electron. Syst., 57 (5), 3071-3083.
699 https://doi: 10.1109/TAES.2021.3069027.

Liu, Y., Zhu, S., Cui, P., et al., 2017. Hopping trajectory optimization for surface exploration on small bodies. Adv. Space Res. 60, 90-102. https://doi.org/10.1016/J.ASR.2017.04.001.

Montenbruck, O., and Gill, E., 2000. Satellite Orbits: Models, Methods, and Applications, Berlin Heidelberg: Springer, pp. 241-243.

Saito, J., Miyamoto, H., Nakamura, R., et al., 2006. Detailed images of asteroid 25143 Itokawa from Hayabusa, Science, 312 (5778), 1341-1344. https://doi.org/10.1126/science.1125722.

Shen, H., Seywald, H., and Powell, R., 2010. Desensitizing the Minimum-Fuel Powered Descent for Mars Pinpoint Landing. J. Guid. Control Dynam. 33 (1), 108–115. https://doi: 10.2514/1.44649.

Shen, H., Zhang T., Li, Z., Li, H., 2017. Multiple-hopping trajectories near a rotating asteroid. Astrophys. Space Sci. 362 (3), 1-9. https://doi.org/10.1016/j.paerosci.2019.06.002.

Tardivel, S., Scheeres, D., Michel, P., et al., 2014. Contact motion on surface of asteroid, J. Spacecraft Rock. 51 (6), 1857-1871. https://doi.org/10.2514/1.A32939.

Tsuda, Y., Saiki, T., and Terui, F., 2020. Hayabusa2 mission status: Landing, roving and cratering on asteroid Ryugu. Acta Astronaut. 171, 42-54. https://doi.org/10.1016/j.actaastro.2020.02.035.

Ulamec, S., Kucherenko, V., Biele, J., et al., 2011. Hopper concepts for small body landers. Adv. Space Res., 47, 428–439. https://doi.org/10.1016/j.asr.2010.09.013

Upadhyay, S., and Aguiar, A., 2019. Local trajectory generation for hopping robots exploring celestial bodies. 2019AIAA Science and Technology Forum and Exposition (SciTech), San Diego, CA. https://doi.org/10.2514/6.2019-1913.

Ushijima, M., Kunii, Y., Maeda, T., et al., 2017. Path planning with risk consideration on hopping mobility. In: IEEE/SICE International Symposium on System Integration (SII), Taipei, Taiwan. https://doi.org/10.1109/SII.2017.8279302.

Van wal, S., Tardivel, S., Scheeres, D., 2017. Parametric study of ballistic lander deployment to small bodies. J. Spacecraft Rock. 54, 1330-1355. https://doi.org/10.2514/1.A33832.

Van wal, S., Tsuda, Y., Yoshikawa, K., et al., 2018. Prearrival deployment analysis of rovers on hayabusa2 asteroid explorer. J. Spacecraft Rock., 55, 797-816. https://doi.org/10.2514/1.A34157.

Veverka, J., et al., 2001. Imaging of small-scale features on 433 Eros from NEAR: Evidence for a complex regolith. Science, 292, 484 - 488. https://doi.org/10.1126/science.1058651.

Wen, T., Zeng, X., Circi, C., and Gao, Y., 2020. Hop Reachable Domain on Irregularly Shaped Asteroids. J. Guid.

729 Control Dynam. 43 (7), 1269-1283. https://doi.org/10.2514/1.G004682.
730 Werner, R., and Scheeres, D., 1996. Exterior gravitation of a polyhedron derived and compared with harmonic and
731 mascon gravitation representations of asteroid 4769 Castalia. Celestial Mech. Dyn. Astron. 65, 313-344.
732 https://doi.org/10.1007/BF00053511.
733 Witte, L., Roll, R., Biele, J., et al., 2016. Rosetta lander Philae–Landing performance and touchdown safety
734 assessment. Acta Astronaut. 125, 149-160. https://doi.org/10.1016/j.actaastro.2016.02.001.
735 Yano, H., Kubota, T., Miyamoto, H., et al., 2006. Touchdown of the hayabusa spacecraft at the muses sea on Itokawa.
736 Science, 312, 1350-1353. https://doi.org/10.1126/science.1126164.
737 Yoshimitsu, T., Kubota, T., Nakatani, I., et al., 2003. Micro-hopping robot for asteroid exploration. Acta Astronaut.
738 52, 441–446. https://doi.org/10.1016/S0094-5765(02)00186-8.
739 Yu, Y., Baoyin, H., 2015. Modeling of Migrating Grains on Asteroid's Surface. Astrophys. Space Sci. 1355 (1) 43-
740 56. https://doi.org/10.1007/s10509-014-2140-3.
741 Yuan, X., Yu, Z., Cui, P., et al., 2018. Probability-based hazard avoidance guidance for planetary landing. Acta
742 Astronaut. 144, 12-22. https://doi.org/10.1016/j.actaastro.2017.11.039.
743 Zhang, Y., Zeng, X., Circi, C., Vulpetti, G., 2019. The motion of surface particles for the asteroid 101955 Bennu.
744 Acta Astronaut. 163, 3-10. https://doi.org/10.1016/j.actaastro.2018.11.044.
745 Zhang, Y., Li, J., Zeng, X., 2021. The dynamical environments analysis of surface particles for different shaped
746 asteroids. Adv. Space Res., 67 (10), 3328-3342. https://doi.org/10.1016/j.asr.2021.02.013.